

Ultraviolet/Visible Quasicylindrical Waves on Semimetal Cd₃As₂ Nanoplates

Zhaohang Xue, Wenzhuang Zheng, Yaolong Li, Mengfei Xue, Aiqin Hu, Junyan Chen, Shangtong Jia, Jinglin Tang, Jianing Chen, Jinlong Du, Peng Gao, Mengxin Ren, Shufeng Wang, Yunquan Liu, Hong Yang, Zhimin Liao, Guowei Lu,* and Qihuang Gong

Resolving the photonic modes in real space is essential to understand the fundamental process and control of photonic behavior in optoelectric devices. However, the understanding of the photonic modes of semimetal Cd₃As₂ is still lacking. Herein, the quasicylindrical waves (QCW) on Cd₃As₂ nanoplates using photoemission electron microscopy (PEEM) are found out. The QCW is due to the optical field scattered by subwavelength indentations, with wavelength being the same as the incident light, and their amplitude decays as $r^{-1/2}$ from the edges. The transverse magnetic (TM) mode dominates the observed QCW of Cd₃As₂ nanoplates, which is affected by the edge structure. In broadband from UV to visible, the QCWs on Cd₃As₂ nanoplates are observed. Further, nanostructures to achieve subwavelength focusing and interference lattice of the Cd₃As₂ optical QCW are achieved. These findings demonstrate the regulation of QCW, which benefits optimizing the optoelectronic performances of semimetal materials in the future.


1. Introduction

An in-depth investigation of photonic modes of nanomaterials facilitates understanding the fundamental process and promotion of performances of optoelectric devices.^[1] Steering the local photonic density of states via nanostructuring is a vital way to optimize and further engineer the performances of optoelectronic devices. As kinds of photonic modes, the surface waves have attracted significant research interest, including surface plasmon polaritons (SPPs) and quasicylindrical waves (QCW).^[2–7] The QCW is an optical field scattered by subwavelength indentations, with radiative and evanescent field components that spread along the surface over a distance of several wavelengths.^[8–11] Extraordinary optical transmission for

Z. Xue, W. Zheng, Y. Li, A. Hu, J. Chen, S. Jia, J. Tang, S. Wang, Y. Liu, H. Yang, Z. Liao, G. Lu, Q. Gong
State Key Laboratory for Mesoscopic Physics
Collaborative Innovation Center of Quantum Matter
Frontiers Science Center for Nano-Optoelectronics
School of Physics
Peking University
Beijing 100871, China
E-mail: guowei.lu@pku.edu.cn

M. Xue
Wenzhou Institute
University of Chinese Academy of Sciences
Wenzhou 325001, China

M. Xue, J. Chen
School of Physical Sciences
University of Chinese Academy of Sciences
Beijing 100049, China

 The ORCID identification number(s) for the author(s) of this article can be found under <https://doi.org/10.1002/adpr.202100354>.

© 2022 The Authors. Advanced Photonics Research published by Wiley-VCH GmbH. This is an open access article under the terms of the Creative Commons Attribution License, which permits use, distribution and reproduction in any medium, provided the original work is properly cited.

DOI: 10.1002/adpr.202100354

M. Xue, J. Chen
Institute of Physics
Chinese Academy of Sciences and Beijing National Laboratory for Condensed Matter Physics
Beijing 100190, China

J. Chen
Songshan Lake Materials Laboratory
Dongguan 523808, China

J. Du, P. Gao
Electron Microscopy Laboratory
School of Physics
Peking University
Beijing 100871, China

M. Ren
The Key Laboratory of Weak-Light Nonlinear Photonics
Ministry of Education
School of Physics and TEDA Applied Physics Institute
Nankai University
Tianjin 300071, China

M. Ren, S. Wang, Y. Liu, H. Yang, G. Lu, Q. Gong
Collaborative Innovation Center of Extreme Optics
Shanxi University
Taiyuan, Shanxi 030006, China

S. Wang, Y. Liu, H. Yang, G. Lu, Q. Gong
Peking University Yangtze Delta Institute of Optoelectronics
Nantong, Jiangsu 226010, China

high-density hole arrays on metal film is attributed to the interactions between the SPPs and QCW.^[5,6] A cross conversion between SPPs and QCW was found on textured metallic surfaces.^[3] Surface wave modes on the interface can transfer the electromagnetic energies at lateral dimensions, supporting device miniaturizations beyond the diffraction limit.

As a 3D analog of graphene, cadmium arsenide (Cd_3As_2) is a 3D Dirac semimetal with novel topological and optoelectronic properties.^[12–15] For example, the intrinsic optical properties of Cd_3As_2 show great potentials in optoelectronic applications, such as highly nonlinear optical coefficients,^[16] saturable absorbers for ultrafast midinfrared lasers,^[17] modulators with ultrafast transient time,^[18,19] and room-temperature broadband photodetectors.^[20] However, due to the limit of the spatial resolution of optical microscopes in previous studies, there is less information on the photonic modes in Cd_3As_2 materials. To optimize the performances of Cd_3As_2 optoelectronic devices, we need to reveal the photonic modes in Cd_3As_2 nanostructures, such as exciton–polaritons (EP), SPPs, and QCWs. In general, Cd_3As_2 cannot support SPPs in the UV or visible range because it has low free carrier density like graphene. A large imaginary part of the Cd_3As_2 refractive index causing high loss hinders the formation of waveguide modes or EP modes.^[21] Hence, the Cd_3As_2 nanoplate should support QCW modes only.

Up to now, several state-of-the-art techniques, such as scanning ultrafast electron microscopy (SUEM),^[22] scanning near-field optical microscopy (SNOM), electron energy loss spectroscopy (EELS), and cathodoluminescence nanoscopy, have been demonstrated as powerful tools for studying electromagnetic waves on the nanoscale. In addition, photoemission electron

microscopy (PEEM)^[23–29] is a non-scanning high-spatial-resolution instrument that collects photoelectrons to image. The PEEM is a powerful tool for studying the surface wave modes of materials. The semimetal Cd_3As_2 has a work function of ≈ 4.5 eV and high optical nonlinear coefficient,^[16] which benefit for imaging the surface wave patterns by the photoemission process. In this situation, we propose the Dirac semimetal Cd_3As_2 as a material platform to investigate pure QCW modes in nanoscale.

Here, we use the PEEM to investigate the optical QCW on Cd_3As_2 nanoplates in broadband from UV to visible. The QCW has the same wavelength as the incident light and has $r^{-1/2}$ decay from the scattering source. The transverse magnetic (TM) modes dominated the QCW pattern, depending on the excitation polarization with respect to the Cd_3As_2 nanoplates edges. The QCW is also affected by the structure of Cd_3As_2 nanoplates. The scattering-type SNOM measurements confirm the optical QCW either. Furthermore, nanostructures on the nanoplates are elaborately designed to manipulate the QCW to realize sub-wavelength focusing and interference light lattice. We also demonstrate numerically that the Cd_3As_2 metasurface can enhance the absorption compared with bare nanoplates. The regulation of optical QCW upon Cd_3As_2 nanoplates lays a foundation for optimizing the performance of Cd_3As_2 optoelectronic applications in the future.

2. Results

Figure 1a shows the schematic of PEEM measurements. A typical Cd_3As_2 nanoplate, as shown in Figure 1b, was synthesized by a chemical vapor deposition (CVD) method.^[30,31]

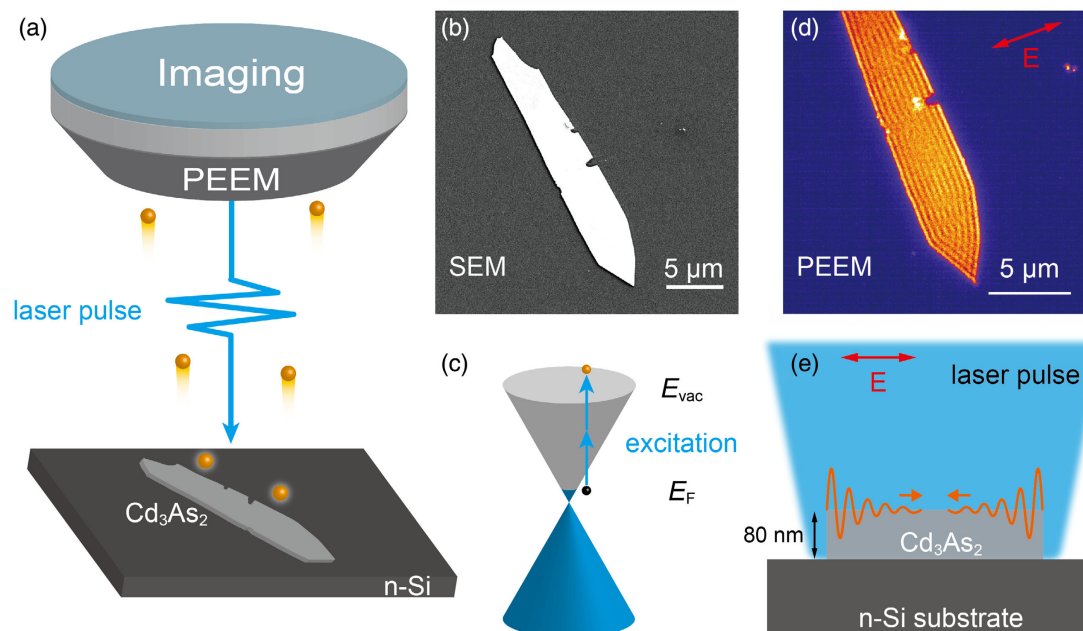


Figure 1. Observation of Cd_3As_2 optical QCW. a) Schematic of the PEEM measurement. Photoelectrons are excited by the laser pulse and collected by PEEM. b) SEM image of the Cd_3As_2 nanoplate. c) Energy diagram of the photoemission process. E_F and E_{vac} denote the Fermi- and vacuum-level energies, respectively. d) Static PEEM image of the same Cd_3As_2 nanoplate illuminated by 410 nm laser pulse. Distinct optical QCW is derived from the sharp edge of the Cd_3As_2 nanoplate. e) Schematic of optical QCW.

The synthesized nanoplates are transferred to the n-doped silicon wafer by a mechanical transfer method.^[32] Figure 1b presents a scanning electron microscopy (SEM) image of the Cd₃As₂ nanoplate, which shows the high quality and uniformity of the Cd₃As₂ nanoplate. The characterizing results of Cd₃As₂ nanoplates by energy-dispersive X-ray spectroscopy (EDS), Raman scattering, atomic force microscopy (AFM), spectroscopic ellipsometry, and EELS measurements are shown in Figure S1, S2, and S3, Supporting Information. The doped 3D Dirac semimetal Cd₃As₂ nanoplates have high electron mobility. The Fermi level is at ≈ 200 meV above the Dirac point,^[12,30] as indicated by the blue-filling area in Figure 1c. The samples are placed at the main chamber of the PEEM system with an ultrahigh vacuum (nearly 1×10^{-10} torr). The laser pulse (pulse duration: ≈ 120 fs) is focused onto the sample at normal incidence and excites the photoelectrons through the photoelectric effect. For $\lambda = 410$ nm pulsed laser (photon energy: 3.02 eV), the photoelectrons emit to the vacuum via a multiphoton process from the Fermi energy of Cd₃As₂ (Figure 1c). The red arrow in the image indicates the polarization of light. The collected photoelectrons generate an image, which is presented in Figure 1d with false color.

Interestingly, there are distinct surface patterns upon the Cd₃As₂ nanoplate due to the QCW. We note that the QCW can be excited efficiently when laser polarization is p-polarized (TM) to the edges. Figure 1e illustrates the experiment diagram: the 410 nm laser pulse is scattered by the sharp edge of the Cd₃As₂ nanoplate and forms QCW. The radiative and evanescent QCW spreads along the sample surface over several wavelengths distance. The optical QCW from both edges of the Cd₃As₂ nanoplate propagates upon the entire Cd₃As₂ nanoplate surface in Figure 1e. The QCWs from the sample edges overlap and form an interference pattern on the surface.

We refer to the finite-difference time-domain (FDTD) framework^[2] and simulate the optical QCW field, as shown in **Figure 2a**. A 100 nm-thick Cd₃As₂ nanoplate is placed on the silicon substrate. A 300 nm \times 300 nm total-field/scattered-field (TF/SF) boundary (dashed rectangle) covers a 100 nm-wide Cd₃As₂ groove. The TF/SF in the rectangle contains the normally incident TM-polarized 410 nm planewave and the scattered field from the groove. The scattering field in the vacuum outside the rectangle (Figure 2a) is a distinct QCW pattern, with wavelength equal to the wavelength of the incident light, and has $r^{-1/2}$ decay from the source (Figure 2b inset). In addition, the silicon substrate also contains a scattered QCW pattern with a wavelength of ≈ 80 nm ($410 \text{ nm}/n_{\text{silicon}}$). The E_x component of QCW interferes with the incident laser pulse (pulse duration: ≈ 120 fs), forming surface waves observed on Cd₃As₂ nanoplates in the experiment. We can draw the E_x component attenuation along the Cd₃As₂-vacuum interface in Figure 2b. The E_y component (Figure 2b blue line) of QCW along the interface excited by the s-polarized (TE) planewave is much weaker than the E_x component excited by the TM planewave. This explains that QCW is excited efficiently by the TM-polarized laser in the experiment. The red dashed line in Figure 2b is given by the analytic form $E_x(x, z)$ equation.

$$E_x(x > 0, 0) = E_{0,0}(x/\lambda)^{-m} \exp(ik_0x) \quad (1)$$

where $E_{0,0}$ is constant. m is a damping exponent to be fit. The exponential part ($\exp(ik_0x)$) describes the amplitude oscillations of the

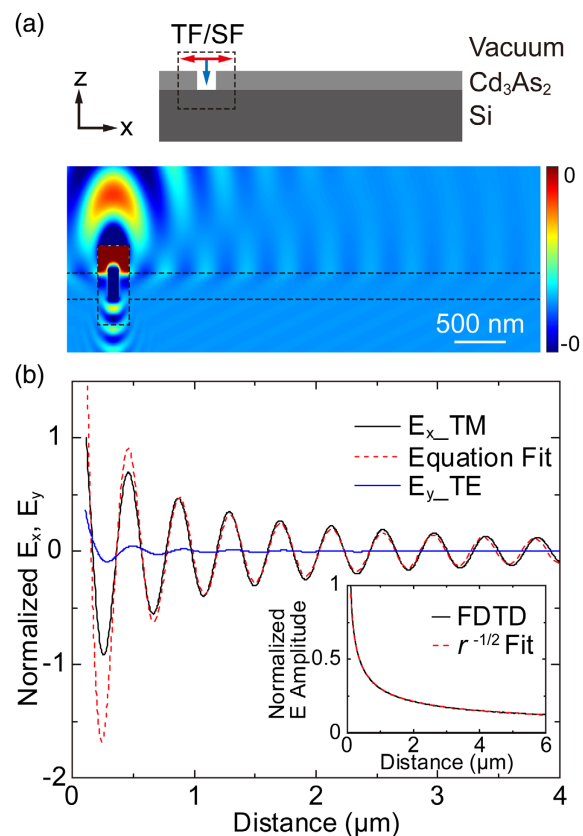


Figure 2. FDTD simulations of the Cd₃As₂ optical QCW. a) Schematic representation of the FDTD simulations and calculated QCW field diagram of the E_x component for normally incident 410 nm TM planewave scattering at a 100 nm-wide and 100 nm-deep Cd₃As₂ groove on the silicon substrate. (The plot is not in line with the scale bar in the z -direction.) b) Normalized E_x distribution (TM excitation) and E_y distribution (TE excitation) at the Cd₃As₂-vacuum interface versus x -axis from the TF/SF boundary. The red dashed line is given by the analytic form E_x equation. The inset shows the $r^{-1/2}$ decay characteristics of the E field amplitude of the QCW.

E_x component. This equation validates the QCW launched on metal or dielectric surfaces at intermediate distances ($x < 10\lambda$).^[8] The surface E_x component simulated by FDTD is not a perfect QCW attenuation curve, as given by the analytic equation, especially for the first two stripes near the scattering source. Because when x tends to be 0, $E_x(x, z)$ tends to be infinity; that is not physical reality. Nevertheless, the deviation between the FDTD numerical simulations and the analytic equation is acceptable when $x > 2\lambda$.

The EELS characterization of the Cd₃As₂ nanoplate in Figure S3, Supporting Information, proves that the surface waves on Cd₃As₂ observed in this work should not be SPPs. The QCW on the Cd₃As₂ nanoplate with an ITO substrate (Figure S4, Supporting Information) overturns the explanation of the waveguide modes. The results of FDTD simulations prove that the surface waves we observed on Cd₃As₂ nanoplates are QCW. At the metal/vacuum interface, the surface field scattered by the groove contains two parts: SPPs and QCW.^[2-7] Because Cd₃As₂ cannot support the SPPs in the UV-to-visible region,

the surface field excited by the groove on Cd_3As_2 contains QCW only, which allows us to observe QCW unambiguously.

Furthermore, we measure the polarization-dependent QCW upon the nanoplate. The sample measured is $\approx 38 \mu\text{m}$ in length and $3.4 \mu\text{m}$ in width. In the $20 \mu\text{m}$ field of view of the PEEM, we just show a part of this sample. To quantitatively analyze the QCW on the Cd_3As_2 nanoplate, we plot photoemission intensity (PEI) along the white dashed line in **Figure 3a,c**. In the case of vertical polarization excitation, parallel optical QCWs are generated from the upper and lower edges of the Cd_3As_2 nanoplate. As shown from the PEI curve in **Figure 3b**, the QCW has its maximum intensity on the edge of the Cd_3As_2 nanoplate. The wavelength of QCW is 393 nm ($\pm 12 \text{ nm}$), which is extracted from the QCW image by the fast-Fourier transform (FFT) method. The effective wavelength agrees with the excitation wavelength of 410 nm . When we rotate a half-wave plate and change the polarization of laser pulse from vertical to horizontal, the optical QCW is generated from the right edge of the Cd_3As_2 nanoplate (**Figure 3c**). From the right edge, ten QCW stripes can be distinguished and propagate about $4 \mu\text{m}$ into the interior of the Cd_3As_2 nanoplate and then fade away (**Figure 3d**). The left edge of the material is far away from

the field of view, so there is not any QCW from the left in the field of view. All these results mean that only the TM modes can be excited and detected, as shown in **Figure 2b**. The PEEM images under oblique incidence are shown and discussed in **Figure S5**, Supporting Information.

Then, we turn to the QCW patterns on the Cd_3As_2 nanoplate (**Figure 3e**). We can find that the QCW is affected by the structure of the Cd_3As_2 nanoplate. There are 11-striped QCWs (**Figure 3f**) on the Cd_3As_2 nanoplate with a width of $3.9 \mu\text{m}$ (white dashed line marked with “f” in **Figure 3e**). As the width of the nanoplate gradually narrowed, missing QCWs appeared in the middle of the nanoplate (**Figure 3g**). That is due to the destructive interference of the QCW from both sides. As the width of the nanoplate is further reduced, 10-striped, 9-striped... 5-striped QCWs (**Figure 3h**) are formed. The change of QCW patterns with structure width has been simulated (**Figure S6**, Supporting Information). Distinct 9-striped QCWs are excited in a $3.4 \mu\text{m}$ -width nanoplate, while missing QCWs exist in a $3.5 \mu\text{m}$ -width nanoplate due to destructive interference (**Figure S6**, Supporting Information).

Notably, we demonstrate that the QCW can exist in a very broad range, at least from the UV-to-visible spectrum range.

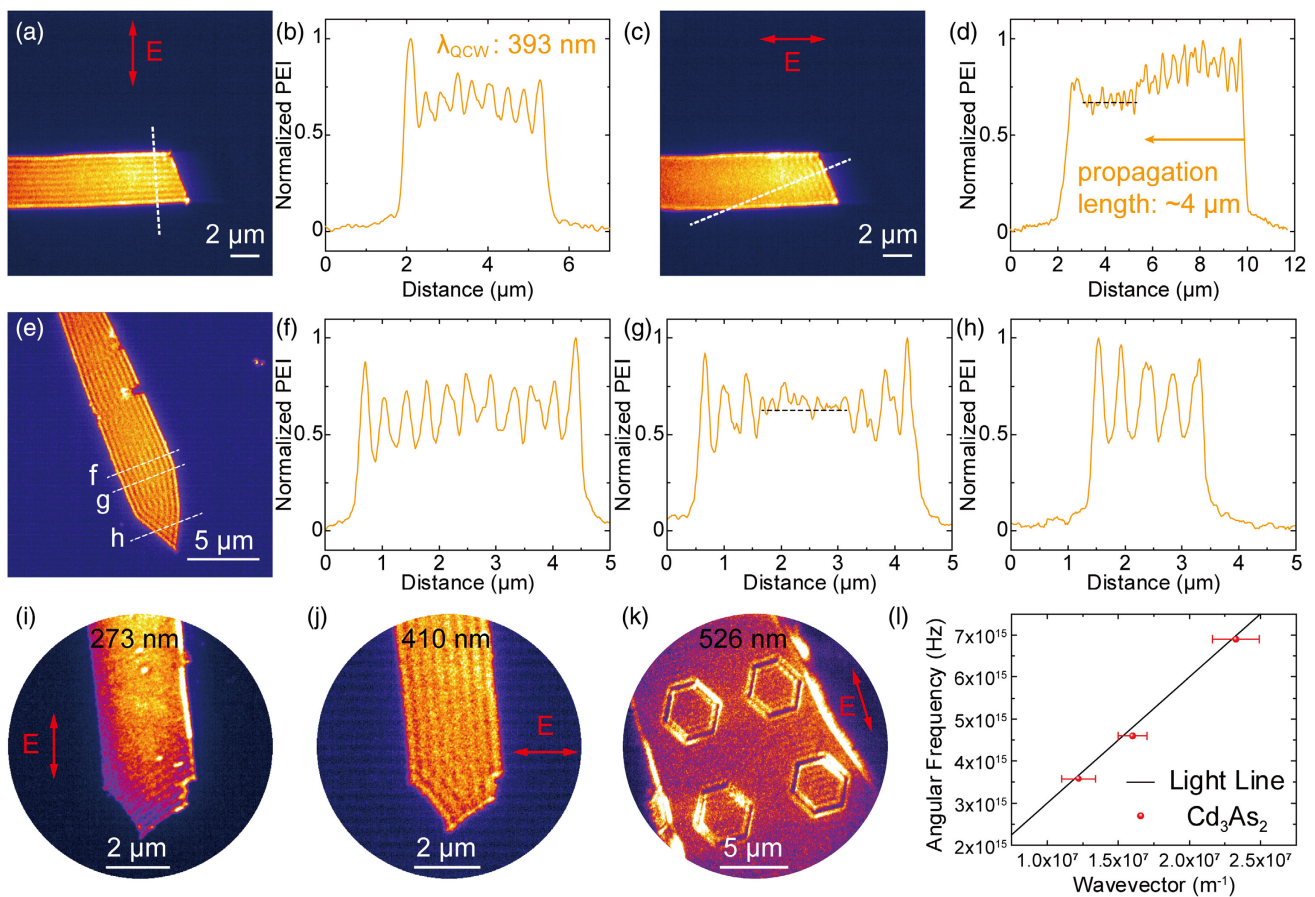


Figure 3. Polarization, structure, and wavelength dependence of Cd_3As_2 optical QCW. Static PEEM image of the same Cd_3As_2 nanoplate illuminated by 410 nm laser pulse with a) vertical and c) horizontal polarizations, as is manifested by the red arrows. b,d) Normalized PEI along the white dashed line in (a, c). e) Static PEEM image in **Figure 1d**. f) The three white dashed lines correspond to 11-striped QCW, g) missing QCW, and h) five-striped QCW, respectively. i–k) Cd_3As_2 optical QCW excited by 273 , 410 , and 526 nm , respectively. The polarization is manifested by the red arrows. l) Dispersion curve of Cd_3As_2 optical QCW.

The optical QCWs have a similar wavelength of 270 nm (± 10 nm) and 515 nm (± 25 nm), as that of excitations by 273 and 526 nm laser pulses, respectively (Figure 3i,k). The optical QCW excited by a 410 nm laser pulse is shown in Figure 3j. Limited by the laser sources and the photoelectric effect, we have only measured Cd_3As_2 optical QCWs under three excitation wavelengths, corresponding to the three red points in the dispersion curve (Figure 3l). As the laser wavelength increases, photon energy decreases, but lower photon energy becomes more difficult beyond the work function through the multiphoton effect (Figure S10, Supporting Information). Taking account of the experimental error, we think that the QCW wavelength is consistent with the excitation light wavelength. This is evidence that the surface waves we observed are the QCW modes.

Next, we design nanostructures to regulate the optical QCW on Cd_3As_2 nanoplates. We fabricate a 4.8 μm -diameter microdisk and another 5 μm -diameter microdisk, using a focused Ga-ion beam. To improve the contrast of optical QCW, we also fabricate two additional concentric rings around the microdisk. The ring lines are 150 nm broad and 410 nm apart. We first use a linear-polarized laser pulse at a wavelength of 410 nm to excite the fabricated surface lens and take the PEEM image, as shown in Figure 4a. The 5 μm -diameter microdisk nanostructure focuses the optical QCW into a bright spot (Figure 4e) with subwavelength size (full width at half maximum (FWHM) is ≈ 240 nm), working as a QCW lens on the nanoplate. In contrast, there is a dark spot at the center of the 4.8 μm -diameter

microdisk (Figure 4d). This is due to deconstructive interference because the diameters of the two microdisks differ by half a laser wavelength, that is 205 nm. The two QCWs generated from the upper and lower edges form a bright (dark) spot in the center of the microdisk due to the constructive (destructive) interference. We can rotate a half-wave plate to regulate the excitation direction of the QCW, as in the movie in the Supplementary Information. When we use a quarter-wave plate to generate a circularly polarized light to excite the sample, the optical QCW becomes a concentric QCW with a dark/bright spot at the centers of the two microdisks (Figure 4b). The optical QCW not only exists inside the nanostructures but can also be excited outside the three concentric rings, as shown in Figure 4a,b.

We also designed a micropolygon nanostructure, and the nanostructure is excited by a linear-polarized 410 nm laser pulse (Figure 4c). The QCW forms a stable optical interface lattice in the polygon, and the nine-striped QCW forms along with the white dashed line (Figure 4f). QCW excited at different edges can also be identified in Figure 4c. The insets in Figure 4d–f show the FDTD images that show good consistency with experiments in Figure 4a–c. The images are calculated from $Y \propto \int (E_{\parallel})^4 dt$,^[33–36] as the fourth power of the in-plane electric field component at the Cd_3As_2 -vacuum interface. The simulated images of the 4.8 μm -diameter microdisk and 5 μm -diameter microdisk have a dark spot and bright spot at the center, whether linearly polarized or circularly polarized excited (Figure S7,

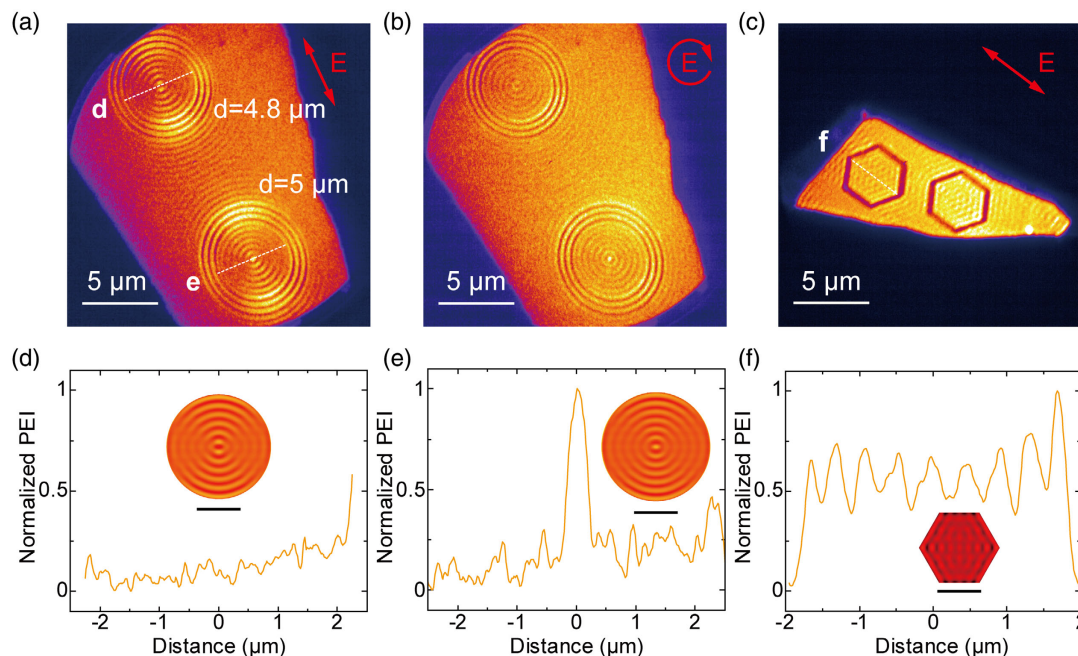


Figure 4. Regulation of Cd_3As_2 optical QCW. a) Static PEEM image of fabricated microdisk nanostructures excited by a linear-polarized 410 nm laser pulse. The polarization is manifested by the red arrow. There is a dark spot at the center of the upper-left 4.8 μm -diameter microdisk, while a bright spot at the center of the lower-right 5 μm -diameter microdisk. b) Static PEEM image of the same Cd_3As_2 nanoplate excited by a circularly polarized 410 nm laser pulse. Concentric waves with a dark/ bright center are formed. c) Static PEEM image of the fabricated micropolygon nanostructures excited by a linear-polarized 410 nm laser pulse. The polarization is manifested by the red arrow. d,e) PEI along the dashed line in the upper-left/ lower-right microdisk with a dark/ bright spot. f) PEI along the dashed line in the micropolygon nanostructure. The insets in (d–f) show simulated PEEM images, consistent with the experiment. The scale bar is 2 μm for the insets.

Supporting Information), which is consistent with the experiment result due to the constructive (destructive) interference.

3. Conclusion

In this article, we use the PEEM to directly visualize the UV/vis broadband optical QCW on Cd₃As₂ nanoplates. The QCW pattern has a wavelength equal to the wavelength of the incident light and has $r^{-1/2}$ decay from the source. The QCW is dominated by the TM mode and is affected by structures of Cd₃As₂ nanoplates. We also realize the interference and subwavelength focusing of the Cd₃As₂ optical QCW by designing nanostructures. The QCW simulated by the FDTD agrees well with the PEEM measurements. After excluding the influence of SPPs and waveguide modes, Cd₃As₂ allows us to observe the optical QCW independently. This work proves a new capability through QCW engineering to improve the on-chip nanophotonic device integration and optical performances based on such semimetal materials.

The QCW, which is usually ignored, can significantly affect the optical performances of devices.^[5,6] The QCW can widely exist on the interface of metals^[2] and dielectric materials such as silicon.^[8] QCW is a kind of nonresonant surface wave; hence, it is effective for broadband. Especially for a high loss dielectric interface, which does not support the SPPs and the waveguide modes, the QCW modes provide a way to steer the local photonic density of states via nanostructuring. In the subsequent work, we intend to use the QCW to enhance the photocurrent response of semimetal Cd₃As₂ nanoplates. For instance, with FDTD simulations (see Figure S9, Supporting Information), we find that the absorption of Cd₃As₂ metasurface reaches 70% compared with 50% of the original Cd₃As₂ nanoplate in broadband. This is beneficial from the assistance of QCW because the constructed interference of incident light and QCW modes results in a higher local field to increase the absorption. These findings pave the way for optimizing the optical performances, such as surface biosensing,^[37] QCW tweezers,^[38] and surface-enhanced Raman spectroscopy (SERS),^[39] through QCW regulation.

4. Experimental Section

Sample Growth and Characterization: The Cd₃As₂ nanoplates were synthesized by the CVD method in a tube furnace.^[30,31] The EDS characterization of Cd₃As₂ nanoplates, which was performed in an FEI Tecnai F20 transmission electron microscopy (TEM), revealed that the elemental molar ratio of Cd:As was 3:2 (Figure S1, Supporting Information). The synthesized Cd₃As₂ nanoplates were transferred to the n-type Si substrate by an XYZ micromanipulator. The (112) surface plane of Cd₃As₂ nanoplates had good quality and was characterized by Raman spectra (Horiba LabRAM HR Evolution) in Figure S2, Supporting Information. The thickness of the Cd₃As₂ nanoplate was 80 nm measured by AFM (Asylum Research Cypher ES, Oxford Instruments) (Figure S2, Supporting Information). SEM images of Cd₃As₂ nanoplates were acquired from electron microscopy (Zeiss Crossbeam 540). The nanostructures on Cd₃As₂ nanoplates were fabricated using an focused ion beam (FIB) milling system (Zeiss Crossbeam 540). The amorphous layer of Cd₃As₂ nanoplates was removed by Ar⁺ etching treatment. Then, the prepared sample was transferred to the preparation chamber of PEEM immediately and annealed under ultrahigh vacuum (below 5×10^{-9} torr) at 180 °C for 1 h to remove any H₂O or impurities absorbed on the sample

surface. The aberration-corrected scanning transmission electron microscopy (STEM) image and EELS data (Figure S3, Supporting Information) were performed using a monochromatic Nion U-HERMES200 electron microscope operated at an accelerating voltage of 60 kV while the convergence semiangle was 20 mrad.^[40,41] The STEM image was acquired with an annular recording range of 80–210 mrad, and the energy resolution of EELS was ≈ 90 meV. Near-field images of Cd₃As₂ optical QCW (Figure S8, Supporting Information) were measured by a commercial scattering-type SNOM (NeaSNOM, Neaspec GmbH) equipped with a visible laser of 532 nm wavelength.^[42,43]

PEEM Measurement: The PEEM measurements were based on a high-resolution PEEM system (SPELEEM, Elmitec GmbH) equipped with an aberration corrector. The femtosecond near-infrared laser pulse (wavelength 820 nm, pulse duration ≈ 100 fs, repetition rate 80 MHz, and output power 2.9 W) output from a commercial Ti: sapphire femtosecond laser system (Mai Tai HP, Spectra-Physics) was used to pump the optical parametric oscillator (OPO; Inspire Auto 100, Spectra-Physics). The second-harmonic generation (SHG) port (410 nm, ≈ 1 W), the signal light port (526 nm, ≈ 180 mW), and the third-harmonic generation (THG) beam (273 nm, ≈ 10 mW) from the fundamental residual laser (820 nm, 1.1 W) were used to excite the photoelectrons, which were collected and hit the fluorescent screen to generate images with a spatial resolution of ≈ 10 nm. The results shown in Figure 3 and 4 were performed when the laser pulses were focused on the sample surface at normal incidence. The results shown in Figure S5, Supporting Information, were performed with 74° oblique incidence. The power dependence measurements of the 410 nm laser (multiphoton absorption) and 273 nm laser (one-photon absorption) are presented in Figure S10, Supporting Information. After passing through the entire optical path, the pulse duration of the laser pulse was ≈ 120 fs, measured by frequency-resolved optical gating (FROG scan MP-001.CX, Mesa Photonics). The lasers were focused on the sample surface with a spot diameter of ≈ 100 μ m. The photoelectrons were collected by a 20 kV static electric field between the sample and the main objective lens of PEEM. To improve the image contrast, we inserted a 50 μ m contrast aperture at the focal plane of the photoelectrons path of PEEM. All the PEEM measurements were performed in the ultrahigh vacuum (below 5×10^{-10} torr) main chamber of PEEM at room temperature.

Supporting Information

Supporting Information is available from the Wiley Online Library or from the author.

Acknowledgements

This work was supported by the National Key Research and Development Program of China (grant no. 2018YFB2200401), the Guangdong Major Project of Basic and Applied Basic Research (grant no. 2020B0301030009), and the National Natural Science Foundation of China (grant nos. 91950111, 61521004, 91850111, and 11527901). In addition, the authors acknowledge the Electron Microscopy Laboratory of Peking University, China, for the use of Cs-corrected Nion U-HERMES200 scanning transmission electron microscope.

Conflict of Interest

The authors declare no conflict of interest.

Author Contributions

Q.G. and G.L. supervised the project. Z.X. conceived the idea, carried out numerical simulations, analyzed the results, and wrote the manuscript text. Z.X., Y.L., A.H., and J.C. performed photoemission electron microscopy measurement. W.Z. and Z.L. fabricated the Cd₃As₂ nanoplates and

discussed the characterization. M.X. and J.C. carried out the scanning near-field optical microscopy measurement. M.R. took part in the spectroscopic ellipsometry measurement. S.J. fabricated nanostructures using the FIB milling system. J.T. measured the Raman spectrum. J.D. and P.G. performed scanning transmission electron microscopy and electron energy loss spectroscopy measurements. J.C., J.D., P.G., S.W., Y.L., H.Y., Z.L., G.L., and Q.G. discussed the results and promoted manuscript presentation. All authors substantially contributed to the manuscript.

Data Availability Statement

The data that support the findings of this study are available from the corresponding author upon reasonable request.

Keywords

Cd₃As₂, nanostructures, photoemission electron microscopy, quasicylindrical waves

Received: November 27, 2021

Revised: December 11, 2021

Published online: January 17, 2022

- [1] T. L. Cocker, V. Jelic, R. Hillenbrand, F. A. Hegmann, *Nat. Photonics* **2021**, *15*, 558.
- [2] L.-M. Wang, L. Zhang, T. Seideman, H. Petek, *Phys. Rev. B* **2012**, *86*, 165408.
- [3] X. Y. Yang, H. T. Liu, P. Lalanne, *Phys. Rev. Lett.* **2009**, *102*, 153903.
- [4] L. Zhang, A. Kubo, L. Wang, H. Petek, T. Seideman, *J. Phys. Chem. C* **2013**, *117*, 18648.
- [5] F. van Beijnum, C. Rétif, C. B. Smiet, H. Liu, P. Lalanne, M. P. van Exter, *Nature* **2012**, *492*, 411.
- [6] H. Liu, P. Lalanne, *Nature* **2008**, *452*, 728.
- [7] C. Sun, J. Chen, W. Yao, H. Li, Q. Gong, *Sci. Rep.* **2015**, *5*, 11331.
- [8] C. H. Gan, L. Lalouat, P. Lalanne, L. Aigouy, *Phys. Rev. B* **2011**, *83*, 085422.
- [9] P. Lalanne, J. P. Hugonin, *Nat. Phys.* **2006**, *2*, 551.
- [10] L. Aigouy, P. Lalanne, J. P. Hugonin, G. Julié, V. Mathet, M. Mortier, *Phys. Rev. Lett.* **2007**, *98*, 153902.
- [11] P. Lalanne, J. P. Hugonin, H. T. Liu, B. Wang, *Surf. Sci. Rep.* **2009**, *64*, 453.
- [12] M. Neupane, S.-Y. Xu, R. Sankar, N. Alidoust, G. Bian, C. Liu, I. Belopolski, T.-R. Chang, H.-T. Jeng, H. Lin, A. Bansil, F. Chou, M. Z. Hasan, *Nat. Commun.* **2014**, *5*, 3786.
- [13] Z. K. Liu, J. Jiang, B. Zhou, Z. J. Wang, Y. Zhang, H. M. Weng, D. Prabhakaran, S. K. Mo, H. Peng, P. Dudin, T. Kim, M. Hoesch, Z. Fang, X. Dai, Z. X. Shen, D. L. Feng, Z. Hussain, Y. L. Chen, *Nat. Mater.* **2014**, *13*, 677.
- [14] J. Cao, S. Liang, C. Zhang, Y. Liu, J. Huang, Z. Jin, Z.-G. Chen, Z. Wang, Q. Wang, J. Zhao, S. Li, X. Dai, J. Zou, Z. Xia, L. Li, F. Xiu, *Nat. Commun.* **2015**, *6*, 7779.
- [15] B.-C. Lin, S. Wang, S. Wiedmann, J.-M. Lu, W.-Z. Zheng, D. Yu, Z.-M. Liao, *Phys. Rev. Lett.* **2019**, *122*, 036602.
- [16] K. Ullah, Y. Meng, Y. Sun, Y. Yang, X. Wang, A. Wang, X. Wang, F. Xiu, Y. Shi, F. Wang, *Appl. Phys. Lett.* **2020**, *117*, 011102.
- [17] Y. Sun, Y. Meng, H. Jiang, S. Qin, Y. Yang, F. Xiu, Y. Shi, S. Zhu, F. Wang, *Opt. Lett.* **2019**, *44*, 582.
- [18] Q. Wang, C.-Z. Li, S. Ge, J.-G. Li, W. Lu, J. Lai, X. Liu, J. Ma, D.-P. Yu, Z.-M. Liao, D. Sun, *Nano Lett.* **2017**, *17*, 834.
- [19] C. Zhu, F. Wang, Y. Meng, X. Yuan, F. Xiu, H. Luo, Y. Wang, J. Li, X. Lv, L. He, Y. Xu, J. Liu, C. Zhang, Y. Shi, R. Zhang, S. Zhu, *Nat. Commun.* **2017**, *8*, 14111.
- [20] M. Yang, J. Wang, J. Han, J. Ling, C. Ji, X. Kong, X. Liu, Z. Huang, J. Gou, Z. Liu, F. Xiu, Y. Jiang, *ACS Photonics* **2018**, *5*, 3438.
- [21] W. Liu, Y. Li, H. Yu, J. Wang, A. Hu, S. Jia, X. Li, H. Yang, L. Dai, G. Lu, Y. Liu, S. Wang, Q. Gong, *Adv. Mater.* **2021**, *33*, 2100775.
- [22] E. Najafi, T. D. Scarborough, J. Tang, A. Zewail, *Science* **2015**, *347*, 164.
- [23] Y. Li, W. Liu, Y. Wang, Z. Xue, Y.-C. Leng, A. Hu, H. Yang, P.-H. Tan, Y. Liu, H. Misawa, Q. Sun, Y. Gao, X. Hu, Q. Gong, *Nano Lett.* **2020**, *20*, 3747.
- [24] A. Hu, X. Xu, W. Liu, S. Xu, Z. Xue, B. Han, S. Wang, P. Gao, Q. Sun, Q. Gong, Y. Ye, G. Lu, *Commun. Mater.* **2020**, *1*, 61.
- [25] L. Wang, C. Xu, M.-Y. Li, L.-J. Li, Z.-H. Loh, *Nano Lett.* **2018**, *18*, 5172.
- [26] M. K. Man, A. Margiolakis, S. Deckoff-Jones, T. Harada, E. L. Wong, M. B. Krishna, J. Madéo, A. Winchester, S. Lei, R. Vajtai, P. M. Ajayan, K. M. Dani, *Nat. Nanotechnol.* **2016**, *12*, 36.
- [27] G. Spector, D. Kilbane, A. K. Mahro, B. Frank, S. Ristok, L. Gal, P. Kahl, D. Podbiel, S. Mathias, H. Giessen, F.-J. Meyer zu Heringdorf, M. Orenstein, M. Aeschlimann, *Science* **2017**, *355*, 1187.
- [28] Y. Dai, Z. Zhou, A. Ghosh, R. S. K. Mong, A. Kubo, C.-B. Huang, H. Petek, *Nature* **2020**, *588*, 616.
- [29] M. Dabrowski, Y. Dai, H. Petek, *Chem. Rev.* **2020**, *120*, 6247.
- [30] C.-Z. Li, L.-X. Wang, H. Liu, J. Wang, Z.-M. Liao, D.-P. Yu, *Nat. Commun.* **2015**, *6*, 10137.
- [31] L.-X. Wang, C.-Z. Li, D.-P. Yu, Z.-M. Liao, *Nat. Commun.* **2016**, *7*, 10769.
- [32] Y. Xiao, C. Meng, P. Wang, Y. Ye, H. Yu, S. Wang, F. Gu, L. Dai, L. Tong, *Nano Lett.* **2011**, *11*, 1122.
- [33] C. Lemke, C. Schneider, T. Leifßner, D. Bayer, J. W. Radke, A. Fischer, P. Melchior, A. B. Evlyukhin, B. N. Chichkov, C. Reinhardt, M. Bauer, M. Aeschlimann, *Nano Lett.* **2013**, *13*, 1053.
- [34] P. Kahl, D. Podbiel, C. Schneider, A. Makris, S. Sindermann, C. Witt, D. Kilbane, M. H.-V. Hoegen, M. Aeschlimann, F. M. zu Heringdorf, *Plasmonics* **2018**, *13*, 239.
- [35] T. J. Davis, B. Frank, D. Podbiel, P. Kahl, F.-J. Meyer zu Heringdorf, H. Giessen, *ACS Photonics* **2017**, *4*, 2461.
- [36] D. Podbiel, P. Kahl, A. Makris, B. Frank, S. Sindermann, T. J. Davis, H. Giessen, M. H.-V. Hoegen, F.-J. Meyer zu Heringdorf, *Nano Lett.* **2017**, *17*, 6569.
- [37] G. Palermo, M. Ripa, Y. Conti, A. Vestri, R. Castagna, G. Fusco, E. Suffredini, J. Zhou, J. Zyss, A. De Luca, L. Petti, *ACS Appl. Mater. Interfaces* **2021**, *13*, 43715.
- [38] C. Min, Z. Shen, J. Shen, Y. Zhang, H. Fang, G. Yuan, L. Du, S. Zhu, T. Lei, X. Yuan, *Nat. Commun.* **2013**, *4*, 2891.
- [39] N. Chen, T.-H. Xiao, Z. Luo, Y. Kitahama, K. Hiramatsu, N. Kishimoto, T. Itoh, Z. Cheng, K. Goda, *Nat. Commun.* **2020**, *11*, 4772.
- [40] L. Zheng, Y. Chen, N. Li, J. Zhang, N. Liu, J. Liu, W. Dang, B. Deng, Y. Li, X. Gao, C. Tan, Z. Yang, S. Xu, M. Wang, H. Yang, L. Sun, Y. Cui, X. Wei, P. Gao, H.-W. Wang, H. Peng, *Nat. Commun.* **2020**, *11*, 541.
- [41] R. Qi, N. Li, J. Du, R. Shi, Y. Huang, X. Yang, L. Liu, Z. Xu, Q. Dai, D. Yu, P. Gao, *Nat. Commun.* **2021**, *12*, 1179.
- [42] M. Xue, M. Li, Y. Huang, R. Chen, Y. Li, J. Wang, Y. Xing, J. Chen, H. Yan, H. Xu, J. Chen, *Adv. Mater.* **2020**, *32*, 2004120.
- [43] X. Lu, O. Khatib, X. Du, J. Duan, W. Wei, X. Liu, H. A. Bechtel, F. D'Apuzzo, M. Yan, A. Buyanin, Q. Fu, J. Chen, M. Salmeron, J. Zeng, M. B. Raschke, P. Jiang, X. Bao, *Adv. Electron. Mater.* **2018**, *4*, 1700377.